



Reduced pressure laser weld comparison to electron beam welds in Ti-6Al-4 V

J. W. Elmer¹ · J. Vaja² · Gordon Gibbs¹

Received: 4 April 2022 / Accepted: 17 July 2022 / Published online: 1 August 2022

This is a U.S. Government work and not under copyright protection in the US; foreign copyright protection may apply 2022

Abstract

Reduced pressure laser welds were made using a 6-kW commercial fiber-laser system on Ti-6Al-4 V and compared to electron beam welds of the same beam diameters as measured by beam diagnostics. The laser welds showed keyhole characteristics under easily achievable mechanical pumped vacuum levels of 1 mbar pressure that nearly matched the electron beam weld penetrations made at 9×10^{-5} mbar vacuum. Ti-6Al-4 V alloys were used to represent refractory metals such as vanadium, tantalum, zirconium, or molybdenum that require vacuum or highly protective inert gas protection systems to prevent adverse interactions with air and can be difficult to weld under non-vacuum conditions. Results show that laser weld depths of 20 mm with aspect ratios of 17:1 can be made under what appears to be stable keyhole behavior as the result of reduced pressure. The effect of fiber diameter was examined using 0.1-, 0.2-, and 0.3-mm fibers, showing that small spot sizes can easily be achieved at long focal length lenses of 400 and 500 mm. The 0.1- and 0.2-mm fibers produced keyhole welds with minimal amounts of porosity, which was only present at 2 kW or higher, while the 0.3-mm fiber produced keyhole welds with more rounded roots that were porosity free as shown by radiography up to the maximum power of 6 kW. Correlations between weld depth and processing conditions are presented for the reduced pressure laser. These results are directly compared to electron beam welds, facilitating design of future reduced pressure laser systems targeted for deep weld penetrations historically developed for electron beams.

Keywords Reduced pressure laser welding · Electron beam welding · Keyhole penetration · Refractory metals · High power density welds · Power density distributions · Root porosity

1 Background and introduction

High power density laser and electron beam sources have been the dominant joining processes for components that require weld precision, minimal heat effects of the base materials, and minimum weld distortion for nearly 50 years [1, 2]. With electron beam welding being done predominantly under high vacuum conditions [2, 3] and laser beam welding being done out of vacuum, the applications for each tended to fall along lines that required vacuum or not. In

addition, even at similar power levels, electron beams were capable of much deeper penetration than lasers, where electron beam welds up to 200 mm in steel [4] and aluminum [5] are possible, while lasers typically would not exceed about 20 mm in depth in steel under similar conditions and have difficulty welding highly reflective materials such as copper and aluminum alloys. Advances in high-power continuous-wave solid-state laser technology with smaller wavelengths in the 1980s tended to broaden the application space for lasers relative to electron beams. However, there were many questions to be asked regarding the advantages and disadvantages of each process and the quality level of high-power laser welds. Lasers tended to be more prone to fusion zone porosity and were still limited to about 20 mm penetration, which was significantly less than would be expected under theoretical heat flow conditions at high power levels [6]. Because of these factors, electron beam versus laser beam differences became one of scientific interest in attempts to understand beam/material interactions, and vacuum level

Recommended for publication by Commission IV – Power Beam Processes

✉ J. W. Elmer
Elmer1@LLNL.GOV

¹ Lawrence Livermore National Laboratory, Livermore, CA, USA

² AWE Aldermaston, Reading, West Berkshire, UK

became one of the most important variables that differentiates the two processes.

Some early work on reduced pressure and vacuum laser welding was performed in the 1980s and 1990s [7–9], showing that the CO₂ laser plume was significantly different and reduced in size for laser welds under reduced pressure, and that weld penetration was enhanced under vacuum. Continued work in the early 2000s by researchers at Osaka University studied the effects of vacuum on laser beam weld penetration and porosity using real-time X-ray radiography unique to their research facility [10]. These studies on stainless steel and aluminum alloys were made using both CO₂ and Nd:YAG lasers and provided direct observations of the beneficial influence of reduced pressure on weld pool dynamics. Their results showed that reduced pressure altered the direction of evaporated metals, altered the laser plasma plume, altered the liquid flow within the weld pool, and reduced the formation of bubbles that could lead to porosity.

Although promising at the time, it took another decade before reduced pressure laser welding started to gain traction when the same group demonstrated deep penetration vacuum laser welds up to 70 mm using an updated laser vacuum system and higher power lasers. Such deep penetration was not possible under atmospheric conditions, and demonstrated that high-power lasers in vacuum can achieve deep keyhole electron beam-like welds [11]. Since then, other researchers have been studying reduced pressure laser welding, and commercial systems are beginning to be developed specifically for this purpose, and scientific interest is growing. For example, Table 1 summarizes the number of publications over the past 20 years from the beginning of reduced pressure laser welding, with less than 50 total technical publications since 2000, compared to several hundred per 5-year period for electron beams and several thousand per 5-year period for conventional laser welding [12]. Reduced pressure laser welding is in its infancy with less than 1% of the total number of annual laser welding publications, but is clearly increasing in number over time, and is expected to grow as more commercial systems become available.

Reduced pressure laser welding, sometimes referred to as vacuum, sub-atmospheric, or low-pressure laser welding, becomes effective at about a 1-mbar soft-vacuum level and requires only mechanical pumping to achieve benefits with little advantage going to lower pressures in most materials

[13, 14]. Reduced pressure laser welds studied so far have been made mostly under laboratory or university settings and often in relatively small, or retrofitted, vacuum chambers to produce demonstration bead-on-plate-type welds with only small amounts of material actually welded. Materials that have been welded by vacuum laser systems include aluminum alloys [11, 15–17], stainless steel [11, 16, 18], steel and galvanized steel [19–22], copper alloys [23], titanium alloys [24], nickel and nickel base alloys [24, 25], and bulk metallic glass [26]. Notable among these metals are copper and aluminum, which are difficult for conventional laser processing and are often welded with electron beam methods. One of the major benefits of vacuum laser welding is the ability to produce deep penetration keyhole type welds. In a side-by-side comparison of reduced pressure laser and electron beam welds in nickel and a titanium alloy, using beam diagnostics to produce as identical beams as possible, the effect of reduced pressure of 10⁻¹ mbar laser increased the depth-to-width aspect ratio in both alloys by nearly 4× compared to atmosphere and matched the depth and aspect ratio of the electron beam welds made at 10⁻⁴ mbar [24]. This was done while significantly reducing, or eliminating, porosity, giving vacuum laser welding true electron beam quality. To date, increased weld penetration has been observed in all reduced pressure laser experimental studies, see for example increased penetration in reduced pressure [11, 27–30], and reduction or elimination of porosity in reduced pressure conditions [10, 11, 24, 31, 32].

Laser welds do not always require deep penetration but nearly all high-quality laser welds require minimal porosity, therefore reduction in porosity may be the major factor in the continued growth of reduced pressure laser welding. During conventional laser welding, laser-induced porosity has been studied with various methods and attempts to reduce porosity include carefully controlling beam conditions, laser plume suppression, shielding gas variations, beam oscillation, and other methods that depended on the laser wavelength, material chemistry, and depth of penetration for success [24, 33–36]. Laser keyhole dynamics models were developed and used to understand laser penetration, laser plume interactions, keyhole stability, and porosity formation in conventional welds [37–42], and have been expanded to understand laser interactions under reduced pressure conditions [14, 18, 30, 43–45]. Based on these studies, the

Table 1 Summary of total publications per 5-year period for reduced pressure laser welding, conventional atmospheric laser welding, and vacuum electron beam welding [12]

Process/years	2000–2005	2006–2010	2011–2015	2016–2020
Reduced pressure laser welding	3	0	10	31
Atmospheric pressure laser welding	1114	1309	2169	3249
Vacuum electron beam welding	117	134	272	452

physical understanding of the beneficial effects of reduced pressure is now well known and is related to a reduction in laser plume interactions, reduced vaporization temperature of the alloy being welded, and modifications to fluid flow within the fusion zone for increased keyhole stability.

With a fundamental understanding of the physical processes responsible for reduced pressure laser material interaction now well established, the challenge becomes one of developing systems that take advantage of this and are robust enough to be commercially viable. As with any new technology, benefits also come with problems that need to be overcome, and it is noteworthy that many of the traditional electron beam welding companies, with decades of vacuum welding experience, have been the first ones offering turnkey laser-in-vacuum systems for welding [46–49]. For reduced pressure laser welding, the challenge is bringing the laser beam into the chamber, which is done using a glass or quartz window that separates the vacuum side of the chamber from the outside where the laser is situated. Windows of this type are common but can become fogged by metal vapors produced during welding. Fogging of the window through vapor or spatter decreases transmission of the laser and can scatter the beam resulting in variable weld penetration, and under extreme conditions can cause overheating of the window to its fracture point. Long focal length lens and/or scanning laser beam optics have been useful to keep the weld as far away as possible from the window to minimize contamination [24].

Proprietary mechanisms for preventing window fogging are being developed by companies who produce reduced pressure or vacuum laser systems, with only a small number of publications discussing the details [50]. The protective systems all work on the principle that reduced pressure laser welds do not need very high vacuum to be effective where approximately 1 mbar (0.1 kPa) is sufficient, and there is little benefit for going to lower pressures [11, 14]. This easily achievable vacuum level allows a side shield of gas to be blown across the face of the window inside the chamber to keep the window clean, while still maintaining a sufficient vacuum for welding using a relatively simple mechanical pump setup, thus avoiding the complexity and cost of high vacuum systems used in electron beam systems [24]. Additional laser vacuum fogging precautions may be required such as internal enclosure with small beam apertures to minimize window contamination for higher power welds or for high vapor pressure alloys [50].

With reduced pressure laser welding now well understood and many of the early problems associated with it resolved, this study builds off of previous work by the same authors in the area of shielding gas effects [51], and vacuum laser welding in small chambers [24]. The goal of this study is to demonstrate high-quality welds in titanium, on a production-ready vacuum laser system, to represent oxygen-sensitive alloys such as Ta, V, Nb, Mo, Zr, and W that are too chemically reactive to be welded with anything other than inert

gasses or vacuum, and to compare these results with traditional electron beam welding that is performed under high vacuum conditions.

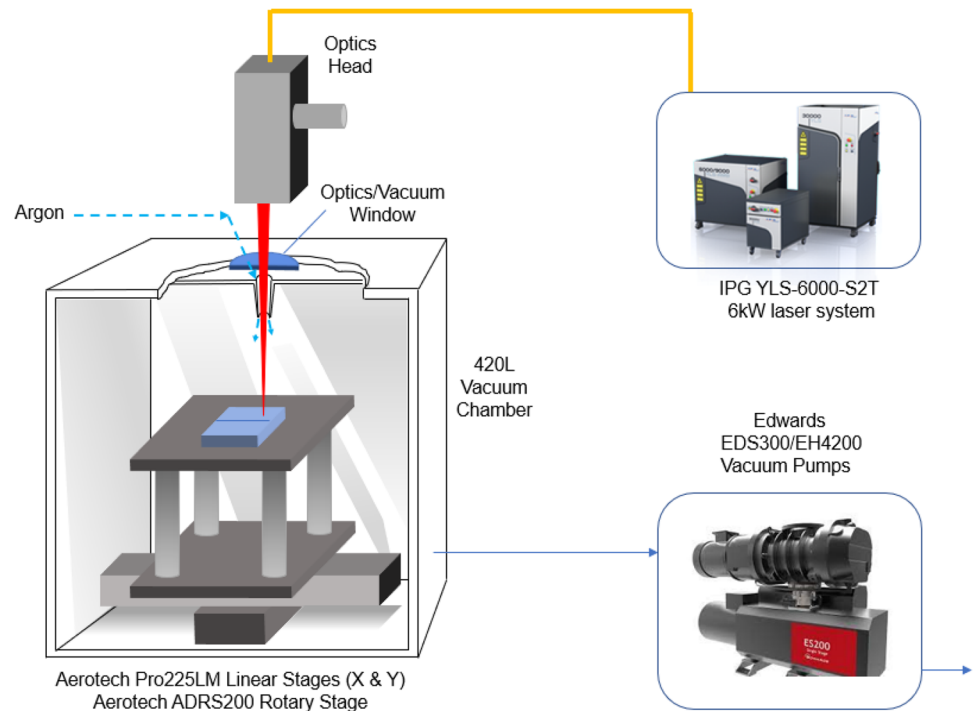
2 Experimental procedures

2.1 Reduced pressure laser welding

An industrial reduced pressure laser system ILiV-420 was procured from InnoLas UK Ltd, based on specifications for production welding, and the laser welds were all made at this facility prior to characterization by AWE. This system is schematically illustrated in Fig. 1 and was designed with a 6-kW IPG-YLS-6000-S2T fiber laser operating at 1.07 μm wavelength, with a 2-mm-mrad beam quality using a 50- μm primary fiber. The 5-m-long primary fiber can be connected directly to the focusing optic head or to a 2-way timeshare unit that allows the beam to be delivered to two workstations with 100 or 200 micron fibers of up to 100 m in length. In the studies performed here, the primary fiber was connected directly to an IPG D50 wobble head, but the beam was not wobbled in this study. The laser system produces a beam quality close to that of high-power electron beams which are on the order of 1 mm-mrad at normal working distances and high voltage [1]. The reduced pressure laser system was designed to operate with three different processing fiber diameters, two different focal length lenses, and a fixed 200-mm collimator, resulting in 6 different optical configurations. The highest power density focused spot would be with the 0.1-mm fiber and 200-/400-mm optics combination (~ 200 mm spot size), while the lowest would be with the 0.3-mm fiber and 200-/500-mm optics combination (~ 750 mm spot size). The system can produce deep welds under reduced pressure for some applications and relatively shallow welds in the 100 to 6000 W power range. A beam switch was incorporated into the system with a provision for two output fibers, where the second fiber could be fitted to another vacuum laser system or conventional workstation in the future. In addition, the laser was fitted with a proprietary laser coupling glass shielding system [52] operating inside the vacuum chamber with co-axial flow of Ar gas.

The reduced pressure chamber measured $750 \times 750 \times 750$ mm and was pumped using a mechanical rotary vane vacuum that can produce controlled vacuum levels from 1 to 150 mbar. This system will pump down to the desired vacuum level in less than 1 min, which is an order of magnitude faster than most electron beam welding machines. Gas flow into the chamber can be controlled from 1 to 15 l/min and the system is set up with automated pump down, venting, and pressure measurements. The equipment motion system uses Aerotech linear and rotational stages and was designed to handle a $250 \times 250 \times 200$ mm size part, with three linear stages having 300 mm travel in x and y , and

Fig. 1 Schematic of the reduced pressure vacuum laser system using 400 or 500 mm focusing optics



200 mm travel in Z with $\pm 10 \mu\text{m}$ accuracy. The fourth axis is a rotary stage with unlimited motion that can be mounted in the horizontal or vertical positions and has a 3-jaw chuck with a 20-kg carrying capacity.

Table 2 summarizes the beam quality measurements and spot sizes for all of the different optical configurations consisting of a 200-mm collimator and either 400- or 500-mm focusing lens, with fibers of 0.1-, 0.2-, and 0.3-mm diameter. The laser beam quality on the new system has a beam parameter product (BPP) as low as 3 mm-mrad (0.1-mm-diameter fiber, 200-/400-mm optics), up to about 10 mm-mrad for the larger fibers, which is similar to the 8.4-mm-mrad BPP used in a previous investigation using a disk laser and small laser vacuum chamber [24].

The laser beams were profiled using a Primes diagnostic to confirm focus position and measure the power density of the beam for different processing fibers and focal length lenses. As an example, Fig. 2 shows the power density distributions for two of the laser beams made with the 0.2- and 0.3-mm fibers and 200/400 optics. Both beams have a top-hat shape

which is characteristic of multimode fiber lasers. The sharp focused beam measured to be 0.39 mm for the 0.2-mm fiber, and 0.58 mm for the 0.3-mm fiber, which are close to the calculated values of 0.4- and 0.6-mm beam diameters. The depth of field as measured by the Rayleigh length, which is the distance away from the sharp focal plane where the beam diameter doubles in size, varies from 3.5 to 14.6 mm, while the half-angle BPP varies between 3.0 and 9.5 mm-mrad depending on the optical configuration. Since the laser beams have a top-hat shape, the peak power density was estimated as the total beam power divided by the beam area, and varies from 2.3 to 31.8 kW/mm^2 , which is a large variation resulting from the different fiber diameters and optical configurations, and is in the range for deep penetration keyhole welding with depth to width aspect ratios greater than unity [1]. In this study, the weld width is measured at 50% of the weld penetration to represent the keyhole width. The peak power density of the beams as measured by the Primes diagnostic is higher than the average values, but had a spiky appearance, where the

Table 2 Optical configurations and beam quality measurements for welds made on the ILiV system at 1 kW power

Collimator/ focus optic	Fiber diameter	Focused beam diameter	Rayleigh length	Avg. power density	Peak power density	M^2	BPP
(mm)	(mm)	(mm)	(mm)	(W/mm^2)	(W/mm^2)	-	(mm-mrad)
200/400	0.1	0.20	3.45	31,800	38,000	8.8	2.97
200/400	0.2	0.39	6.24	8,370	10,000	17.5	5.90
200/400	0.3	0.58	8.82	3,780	5,000	28.1	9.50
200/500	0.3	0.74	14.6	2,300	3,000	27.8	9.35

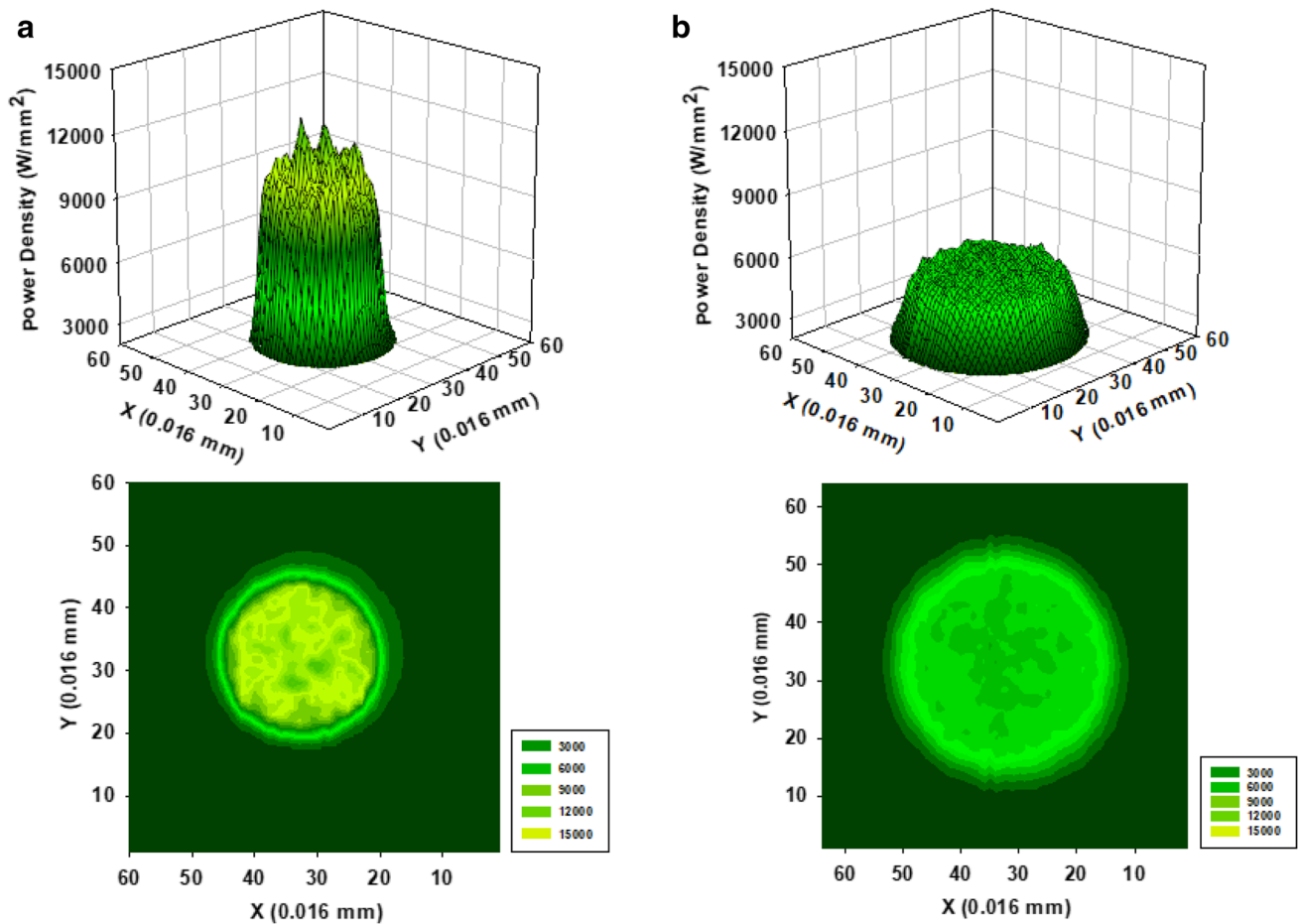


Fig. 2 Power density distribution plots for **a** a 1-kW 0.39-mm-diameter beam (0.2-mm fiber with 200/400 optics) and **b** a 1-kW, 0.58-mm-diameter beam (0.3-mm fiber with 200/400 optics). The x and y axes are 1 mm wide

power density is approximately 20% higher than the average value that was measured over the entire beam, and an estimate of the peak power density spikes is reported in Table 2.

The laser beam welds were made on Ti-6Al-4 V coupons that were 15 mm thick, machined from starting plate stock of nominal Ti-6Al-4 V composition per UNS R56400. For higher power welds, two coupons were stacked on top of each other to allow for penetrations deeper than 15 mm. The welds were all carried out at a reduced pressure of 1 mBar with argon flow of about 10 l/min to protect the laser optics. The travel speed was kept constant at 15.4 mm/s, and the beams were sharp focused on the surface of the plates. A total of 12 welds were made using each of the optical configurations, and the results of the penetrations, weld widths, and aspect ratios are summarized in Table 5.

2.2 Electron beam welding

Electron beam welds were made at LLNL for comparison with the laser vacuum weld geometries and weld quality. The

electron beam welds were made using a 150-kV 50-mA maximum Hamilton Standard machine (No. 605) at 9×10^{-5} mbar (6.8×10^{-5} Torr) vacuum, with the parameters summarized in Table 3. These welds are similar to the electron beam welds made in a previous study [24], and were made at a work distance of 336 mm and 436 mm, which corresponds to effective focal lengths of 400 mm and 500 mm on this machine.

The EMFC electron beam diagnostic was used to characterize the beam as detailed elsewhere [53–56]. Initially, at the 500-mm focal length, a lower accelerating voltage of 85 kV was used to produce the larger 0.59-mm-diameter beam (0.3-mm fiber 200-/400-mm optics), and a high voltage of 145 kV was used to produce the smaller 0.39-mm-diameter beam (0.2-mm fiber 200-/400-mm optics). The beam diameter is measured by the EMFC at the $1/e^2$ height of the Gaussian beam shape, which is sometimes referred to as 4σ and contains 86.5% of the total beam power [56], where σ is the standard deviation of an ideal Gaussian beam. An additional parameter is reported that measures the width of the Gaussian beam at half its maximum peak (FWHM), is

Table 3 Electron beams measured using the EMFC diagnostic at a focal length of 500 mm for 1-kW beams on Hamilton Standard welder No. 605

Effective focal length	Focused beam diameter, $1/e^2$	Beam voltage	Beam current	Beam width, FWHM	Peak power density	Rayleigh length	M^2	BPP
(mm)	(mm)	(kV)	(mA)	(mm)	(W/mm ²)	(mm)	-	(mm-mrad)
500	0.39	145	6.9	0.24	15,318	~30	*	2.44
500	0.58	85	11.8	0.35	7,010	~50	*	3.68

*Calculated M^2 values for electron beams are much larger than lasers due to their smaller effective wavelengths [1]

equal to 2.35σ , and contains 50% of the beam's power [56]. Table 3 further calculates the half-angle BPP of the electron beam, which for a given beam diameter and focal length is smaller than the laser BPP due to the smaller raw electron beam diameter of 12.5 mm at the final focusing lens [24] than the laser that is approximately $2\times$ as large. The smaller divergence angle of the electron beam also results in larger Rayleigh length and smaller BPPs, providing additional depth of focus for the electron beam relative to the laser.

Figure 3 plots the power density distribution as measured by the EMFC for 1-kW electron beams made for two different beam diameters of 0.39 mm (85 kV/11.8 mA) and 0.58 mm (145 kV/6.9 mA) as a comparison to the laser beam profiles shown in Fig. 2. It is clear that the electron beams are largely Gaussian shaped with a sharp peak that differentiates them from the top-hat shape of the multimode fiber laser beams. One characteristic of the difference in shapes is that for a given beam diameter and power, the electron beam achieves

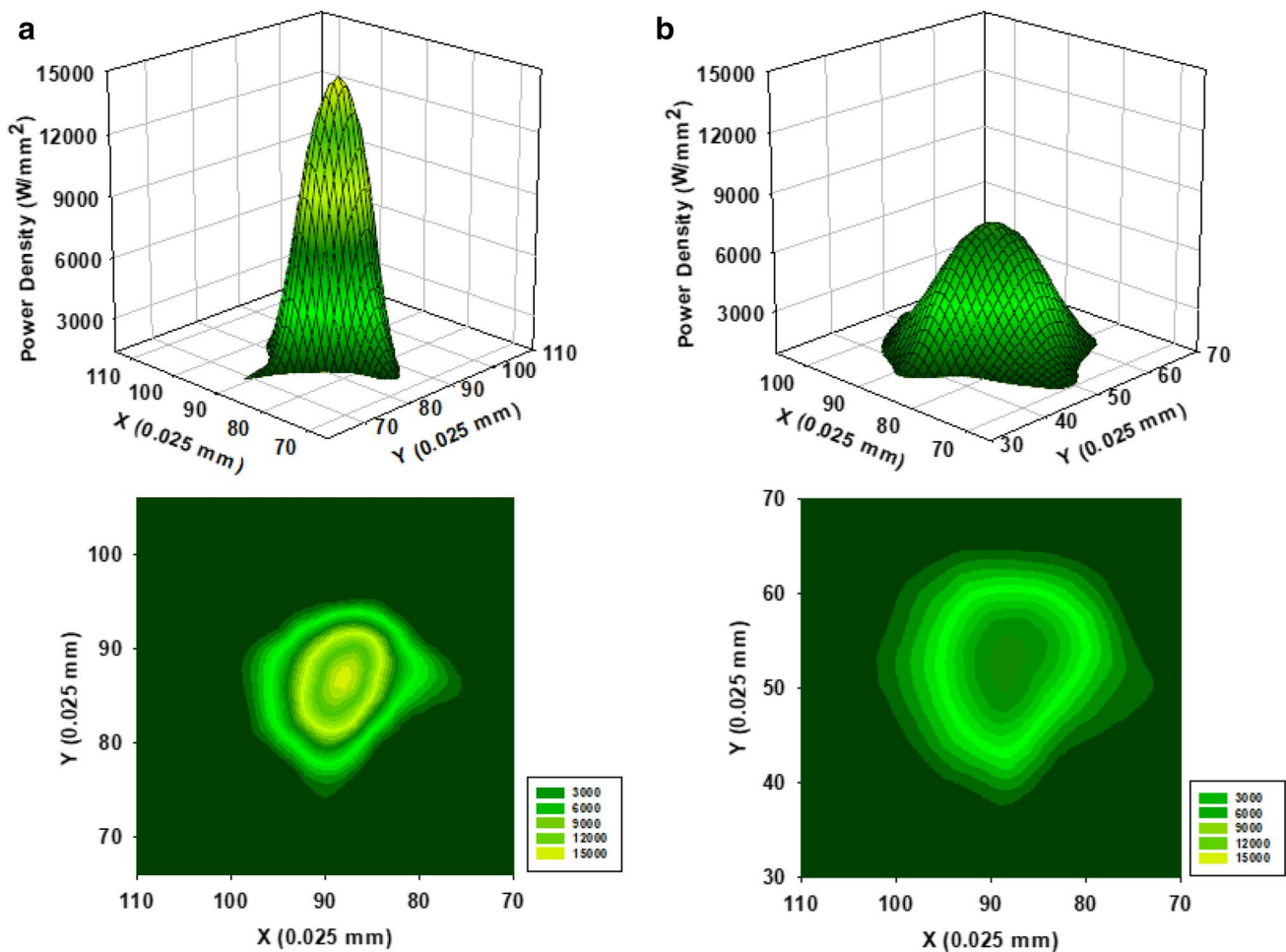


Fig. 3 EMFC power density distribution plots for 1 kW electron beams at a 500-mm focal length for **a** 0.39-mm-diameter beam at 145 kV and **b** 0.58-mm-diameter beam at 85 kV. The x and y axes are 1 mm wide

higher peak power densities as summarized in Table 2 for the reduced pressure laser and Table 3 for the electron beams, where the electron beam has a peak power density of approximately $1.8\times$ that of the laser beam for both conditions.

A series of electron beam welds were made on Ti-6Al-4 V coupons (Ti, 6.09 Al, 4.02 V, 0.01 C, 0.0022 H, 0.25 Fe, 0.007 N, 0.117 O wt%) to demonstrate the influence of beam power on a constant-sized beam for comparison with the reduced pressure laser welds. In order to do this at a fixed working distance, the accelerating voltage of the beam was increased with the beam current to maintain a beam diameter of approximately 0.58 mm (0.3-mm fiber 200-/400-mm optics) throughout the entire power range. The coupons measured $150\times 25\times 9$ mm, and the coupons were welded on the side of the sample so that penetrations up to 25 mm could be investigated. The travel speed was kept constant at 15.4 mm/s, and the beams were sharp focused on the surface of the plates. The beam current and voltage were varied to produce powers from 300 up to 6000 W, while maintaining a constant beam size for the welding experiments to be discussed later with the data summarized in Table 6.

2.3 Characterization

Metallographic samples were prepared by cross sectioning the welds from the plates, grinding and polishing them using conventional metallographic procedures. After final polishing, the Ti-6Al-4 V electron beam welded samples were chemically etched using a modified Kroll's solution containing 5 ml HF, 10 ml HNO₃, and 30 ml lactic acid, while the laser-welded samples were etched in an aqueous solution containing 2% HF acid for approximately 30 s to reveal the details of the weld fusion and heat-affected zones' macrostructures, or 5% HNO₃ and 0.5% HF etchant for microstructural features. Measurements of the weld depth and width were made using a Keyence metallography for low-power welds, or directly on macrographs of the cross sectioned deeper welds that were too large to image on the metallograph.

Computed tomography (CT) 3D imaging was used to inspect the laser-welded samples for internal porosity or other defects. The CT was performed on a Nikon X-Tek XTH225CT cabinet-based CT system with a 225-kV Micro-focus X-ray source that provides a nominal focal spot size of 3 μm (when measured at 70 kV and 0.1 mA) at the X-ray emission point. X-ray images were generated using a tungsten target and were captured by a Perkin Elmer XRD4343CT Amorphous Silicon Flat Panel detector with a cesium iodide scintillator screen, an input screen 430×430 mm in size having 2880×2880 detector elements. This arrangement resulted in a native pixel size of 0.15 mm on the 16-bit detector which has 65,536 gray-levels of dynamic range. A 0.5-mm-thick copper filter was placed between the collimated X-ray source and the detector to enhance the image quality. Data was taken

on weld sections that were placed upon a turntable between the X-ray source and detector and rotated through 360°, with 721 images (projections) being captured at regular angular increments during the rotation. The captured digital radiographs were then processed through a reconstruction algorithm into a 3D CT volume representation of the component. During reconstruction, each pixel from the detector at every angular increment is processed into a 3-dimensional volume element with gray level and position and having a voxel resolution of approximately 0.030 mm size. The CT volumes were then loaded into Volume Graphics V.G Studio Max Version 3.2 to display a 3D rendering of the sample with spatial resolution down to the voxel size for analysis. The reconstructed images were then analyzed using 2D projections, or virtual slices, to determine porosity and porosity distribution within the welded samples.

3 Results and discussion

3.1 Reduced pressure laser keyhole weld penetration

Reduced pressure laser welds were made on Ti-6Al-4 V using different processing fiber and focal length lens combinations with powers up to 6000 W to determine penetration depth, fusion zone geometry, and defect formation for different optical configurations as summarized in Table 2, and welding conditions as summarized in Table 4. The focused beam diameters varied from 0.2 to 0.74 mm using different fibers and focusing lenses in order to test out different options for achieving deep keyhole welds. Longer focal length lenses are desirable as they provide more working distance inside the vacuum chamber, but because they focus to larger spot sizes a careful study was made to see how the longer focal length lenses would work for creating the required penetrations.

The welds were cross sectioned and macrostructures of one set of welds for the 0.58-mm-diameter beam are shown in Fig. 4. In these cross sections, the fusion zone is seen as the innermost portion of the etched weld region and is surrounded by the heat-affected zone (HAZ) that forms by solid-state phase transformations adjacent to the weld fusion zone. The depth of penetration was measured from the plate surface to the fusion zone root and shows that the penetration increases from 2.4 to nearly 20 mm as the power is increased from 700 W to 6 kW. All the welds are deep and narrow with very straight sidewalls at high depth-to-width aspect ratios representative of keyhole penetration conditions. There are no significant visible defects in the cross sections, and they are porosity free, even at the root of the welds, which is exceptional for high aspect ratio high power density welds.

The weld penetration, weld width at half of the keyhole depth, and the aspect ratios of the welds are summarized in

Table 4 Summary of weld parameters and penetration ranges

Weld material	Beam power (kW)	Travel speed (mm/s)	Beam diameter (mm)	Interaction time (d/S) (ms)	Peak power density (kW/mm ²)	Weld depth (mm)
Ti-6Al-4 V laser	0.1–1.0	15.4	0.20	13	6.4–31.8	0.9–6.9
Ti-6Al-4 V laser	0.7–6.0	15.4	0.39	25	5.9–50.2	2.4–19.4
Ti-6Al-4 V laser	0.7–6.0	15.4	0.58	38	2.7–22.7	2.0–18.9
Ti-6Al-4 V laser	0.7–6.0	15.4	0.74	48	1.6–14.0	2.0–17.6
Ti-6Al-4 V EB	0.3–6.0	15.4	0.58	38	2.2–40.6	0.9–20.8

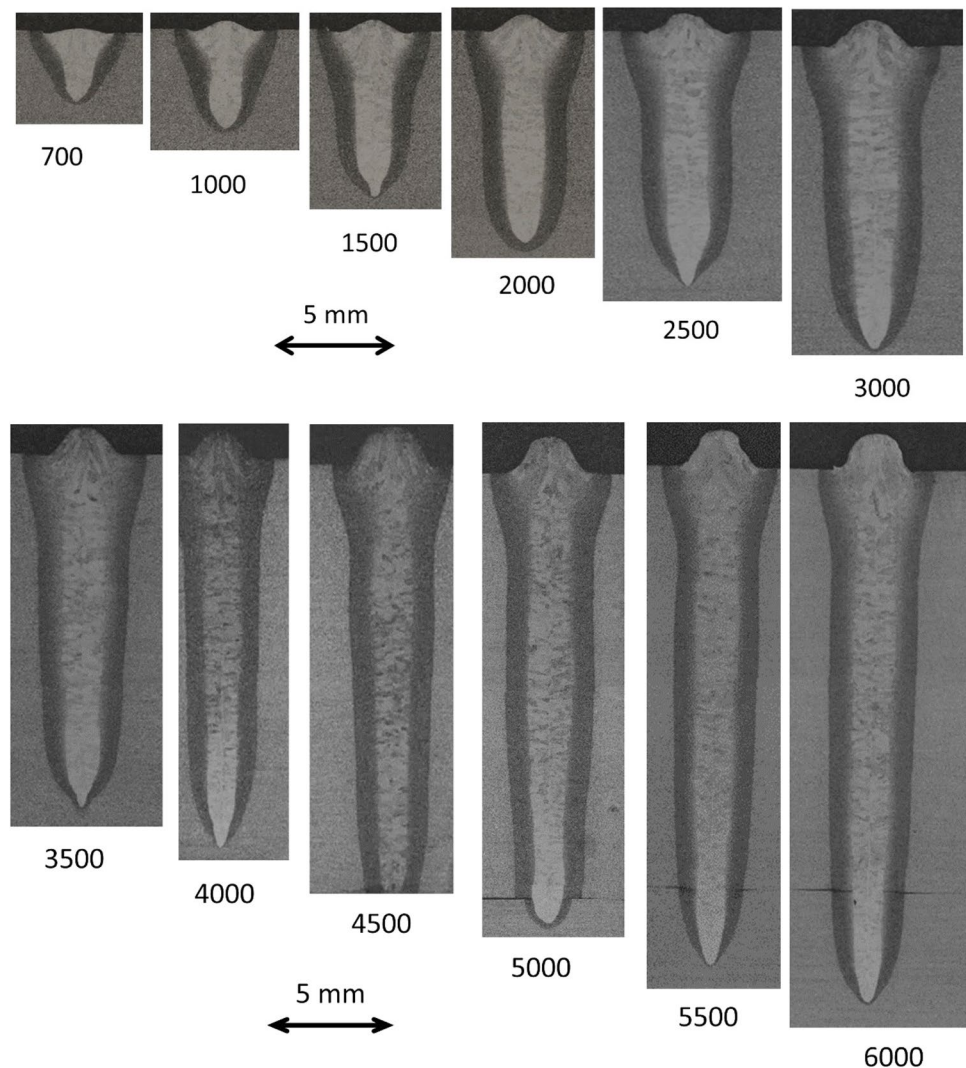
Fig. 4 Reduced pressure laser weld cross sections for the 0.58-mm-diameter beam over the entire power range from 700 to 6000 W

Table 5 in the Appendix. Figure 5 plots the penetration versus three different power factors. Figure 5a plots the penetration data for each of the four optical configurations versus as energy per unit length of weld, P/S , where P is the beam's power and S is the travel speed of the weld, which has been traditionally used for low power density arc welds with the heat distributed mostly on the surface of the weld [57]. Since this factor does not incorporate the beam diameter, the data deviate

considerably, particularly for the smallest diameter beam that has the highest power density. Figure 5b plots the same data versus P/dS . This parameter is sometimes used in a simple model to estimate the effects of changing spot sizes, power, or travel speed on keyhole weld penetration for a given material [58], and has a better fit to the data overall, but still lacks in precision where the penetration varies by over $2\times$ for a given power parameter. Figure 5c plots the same data now versus a

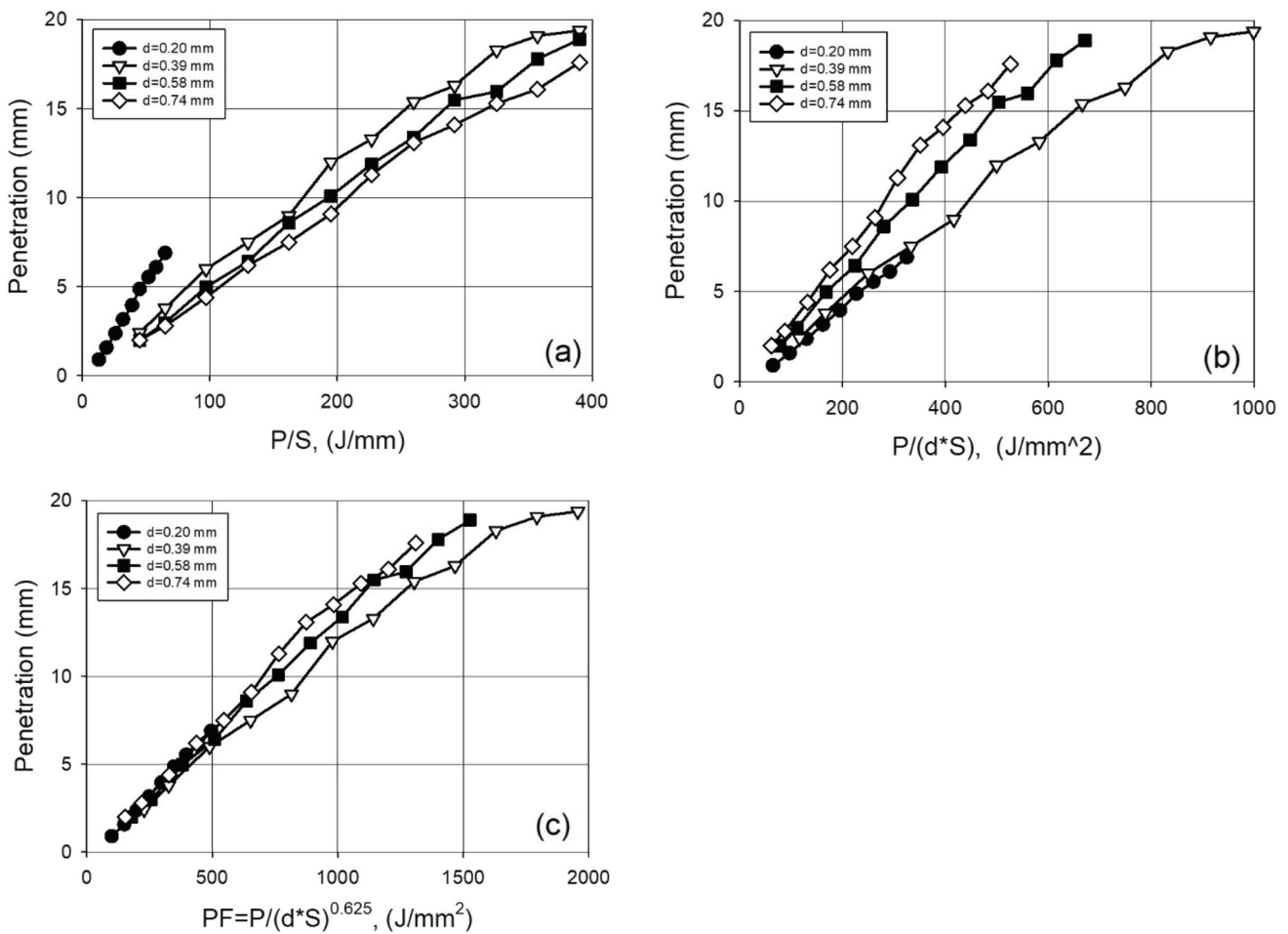


Fig. 5 Summary of weld penetrations for the four different beam diameters on Ti-6Al-4 V at 15.4 mm/s travel speed. Penetration is plotted for **a** as a function of energy per unit length of weld, P/S , **b**

versus $P/(d*S)$, and **c** versus the power law denominator $P_F=P/(d*S)^{0.625}$ per line source fit of keyhole welds. [59]

power factor, $P/(dS)^{0.625}$, which has been used in the past to represent deep keyhole welds that are modeled using the line heat source theory [59]. This factor brings the four different optical configurations into closer alignment, with extremely good matching for penetrations up to about 6 mm but shows some deviations at high penetrations where it predicts deeper penetrations for larger diameter beams at a given power factor. Overall, however, this fit is excellent considering the wide range of power densities (2–50 kW/mm²) with 20× variation in penetration, and will be used here to further analyze the data.

The penetration data is replotted in Fig. 6 versus the power factor, where it is fit with a second-order polynomial and constraint to have 0 penetration at $P_F=0$. From this fit, the penetration can be predicted from the following relationship:

$$d = -2.358 \times 10^{-6} (P_F)^2 + 1.53 \times 10^{-2} (P_F) \tag{1}$$

where the weld depth, D , is in millimeters and is related to the power factor, $P_F=P/(dS)^{0.625}$, for the beam diameter, d in

millimeters, the power, P , in W, and the travel speed, S , in mm/s. The data has an excellent fit showing an R^2 confidence level of 0.989, and the general trend of the data indicates that the penetration increases with the power factor but at a decreasing rate. Heat flow theory for keyhole welds often uses analytical line-source or cylindrical source models to predict weld depth, which suggests that weld penetration would scale directly with weld power for a given alloy and set of welding parameters [6, 59, 60]. More advanced numerical keyhole weld models help to explain deviations from a direct relationship between laser power and depth of penetration that tends to drop off at higher penetration depths [14, 38, 42, 61, 62], and is consistent with the penetration data observed here for reduced pressure laser welds in Ti-6Al-4 V.

3.2 Weld width and keyhole aspect ratios

Keyhole welds are differentiated from conduction welds based on the depth-to-width, D/W , aspect ratios, where keyhole welds

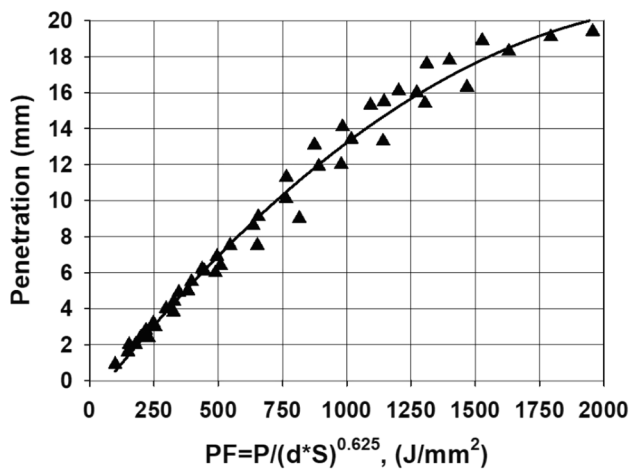


Fig. 6 Fit of all the reduced pressure laser weld penetration data to the power factor $P_F = P/(dS)^{0.625}$ using a 2nd-order polynomial for prediction of weld depth over a wide range of laser parameters

exceed semicircular cross-sectional shapes with $D/W > 0.5$. The phenomena is well documented in the welding literature and results from vapor cavities being generated in high power density welds that distribute the beam's energy below the surface of the plate [1, 2, 61, 62]. The formation, or avoidance, of the vapor cavity requires a critical energy density to vaporize the metal, and conduction welds will be made if the energy density is too low. For example, short duration laser spots are typically made with aspect ratios less than 0.5 [63], and very high-speed electron beam welds can have aspect ratios less than 0.5 [59], and also in additive manufacturing where very high speeds are used to avoid keyholing [64]. At higher energy densities that are produced at typical welding speeds and power densities on the order of 1 kW/mm^2 or higher, depending on the material, a vapor cavity develops and produces the high aspect ratio keyhole welds that were produced in this investigation.

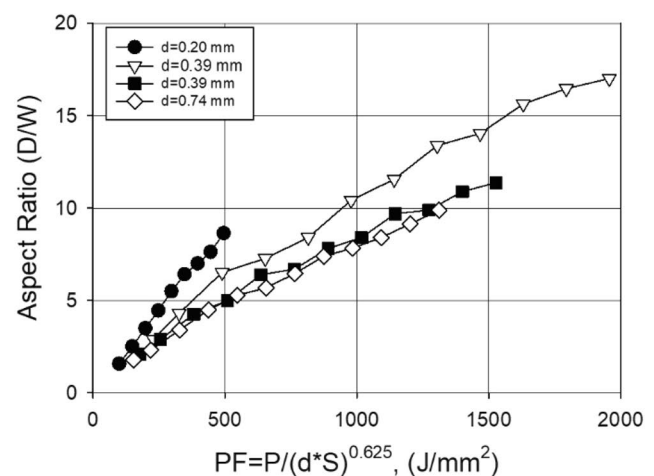
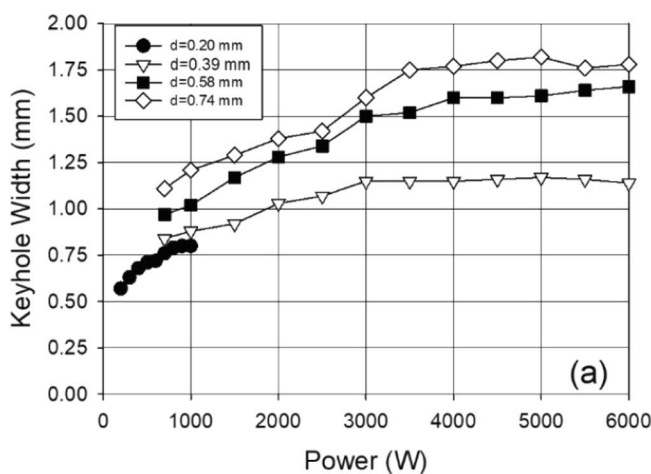


Fig. 7 **a** Keyhole widths as a function of beam power and **b** aspect ratios plotted versus the power factor for each of the laser beam diameters

Figure 4 shows cross sections from one of the series of reduced pressure laser welds with a beam diameter of 0.58 mm and indicated that the weld depth increased significantly with weld power. This figure also indicates that the weld width, measured at 50% of the penetration depth, does not increase in proportion to the weld power or weld depth, thus indicating an increase in the aspect ratio of the weld with increasing power. The weld depth, width, and aspect ratios for all of the laser welds are plotted in Fig. 7, and the measurements are summarized in Table 5. The weld keyhole fusion zone width, Fig. 7a, increases with power up to approximately 3–4 kW, where it then reaches different plateaus depending on the beam diameter. It is clear that a relatively stable keyhole has been established at this point, allowing the beam to drill deeper into the Ti-6Al-4 V base metal with increasing power but not increasing the weld width. Thus, the aspect ratio increases, as indicated in Fig. 7b, which plots the ratio of keyhole depth to width as a function of the power factor shows a constant increase with power from a low value of around 2:1 up to the very high value of 17:1 at 6 kW. The reduced pressure laser welds all display keyhole geometries and demonstrated electron beam-like penetrations throughout the entire power range. The results show that aspect ratios of 10:1 are easily achievable at high powers with the highest aspect ratio of 17:1 demonstrated on the 0.39-mm beam at 6 kW.

3.3 Reduced atmosphere laser weld quality

Deep penetrating high aspect ratio keyhole welds shown above are ideal when minimal heat affects are required on the base metal. However, the high aspect ratio requires more precision to align and follow the weld joint, and can create root spiking and porosity if the beam is too intense³. Keyhole laser welds made under atmospheric conditions and inert gas tend to be porosity prone,

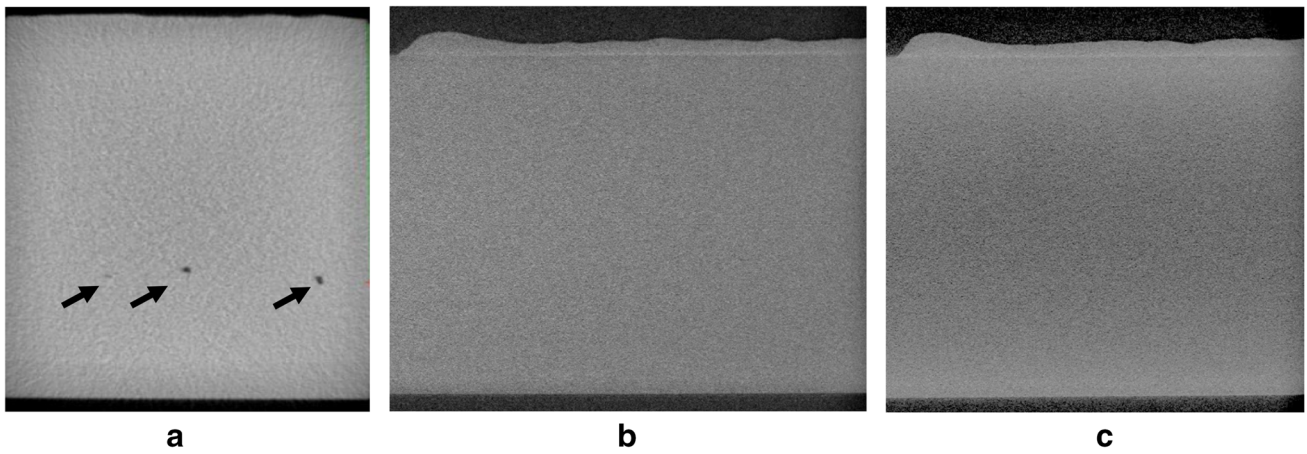


Fig. 8 CT X-ray images showing reduced pressure laser welds for **a** 2500-W, 0.39-mm-diameter beam having occasional root pores; **b** 6000-W, 0.58-mm-diameter laser beam weld with no pores; and **c**

6000-W, 0.74-mm-diameter laser beam weld with no pores. Note the thickness of the 15-mm plate for scale

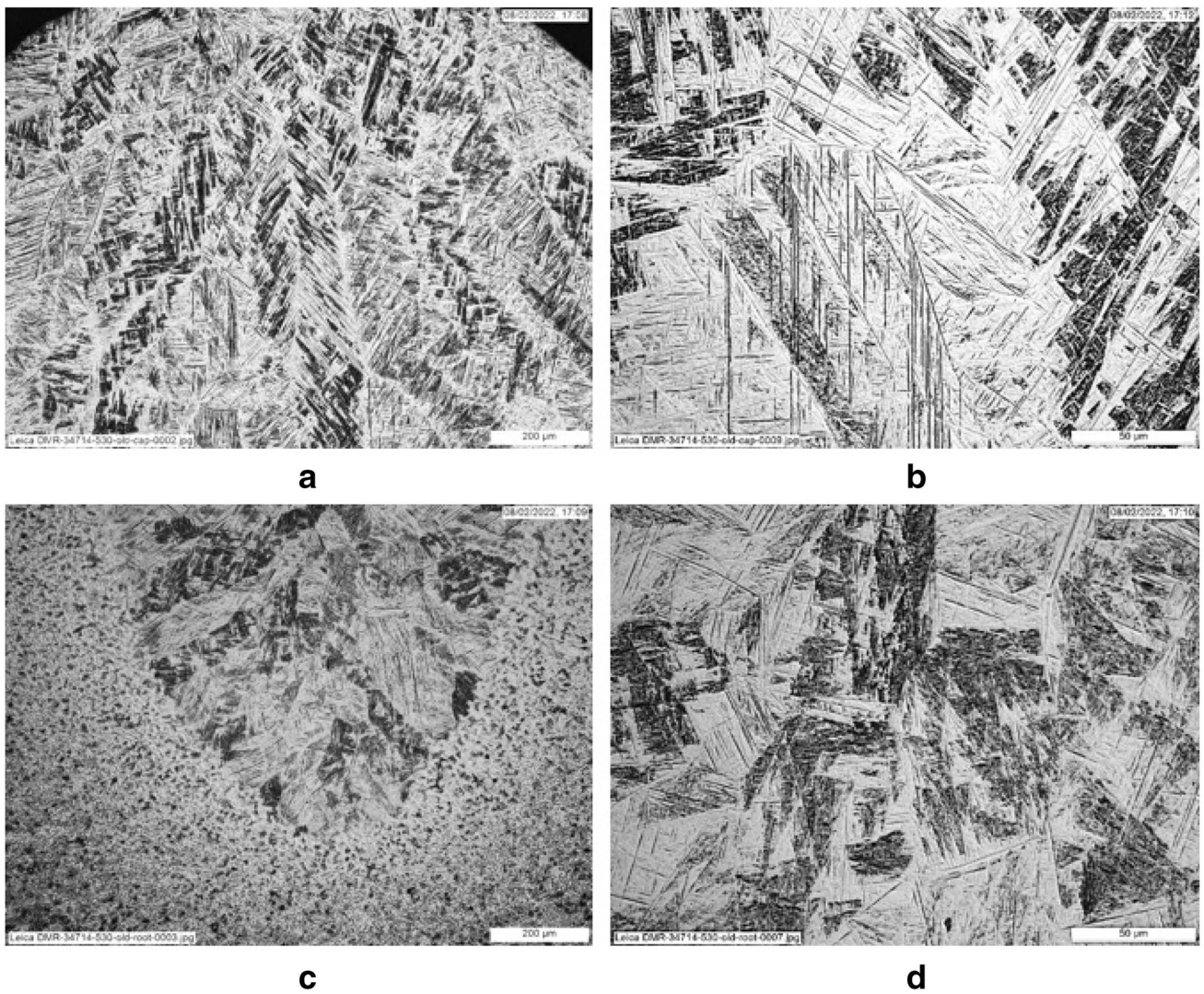


Fig. 9 Reduced pressure laser weld microstructures formed at the crown (**a, b**) and root (**c, d**) in the laser welds. The scale markers (lower right-hand side of images) are 200 mm (**a** and **c**) and 50 mm (**b** and **d**)

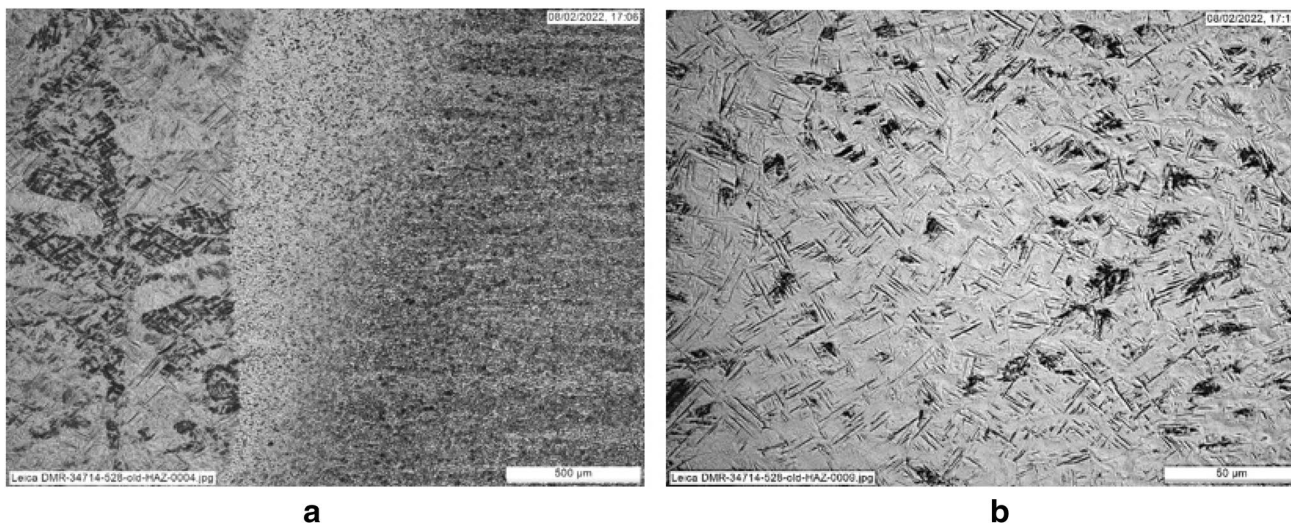


Fig. 10 Fusion zone, HAZ, and parent metal microstructures of the reduced pressure laser weld made at 1000 W at **a** low magnification and **b** higher magnification near the fusion boundary. The scale markers (lower right hand side of images) are 500 mm (**a**) and 50 mm (**b**)

with some reduction in porosity for some alloys using non-inert gas that allows pores to dissolve into the liquid melt pool [51], and particularly under reduced pressure conditions [24, 31, 32].

The results from this investigation confirm the benefits of reduced pressure laser welds on reduced porosity, where minimal porosity was observed, even in the deepest

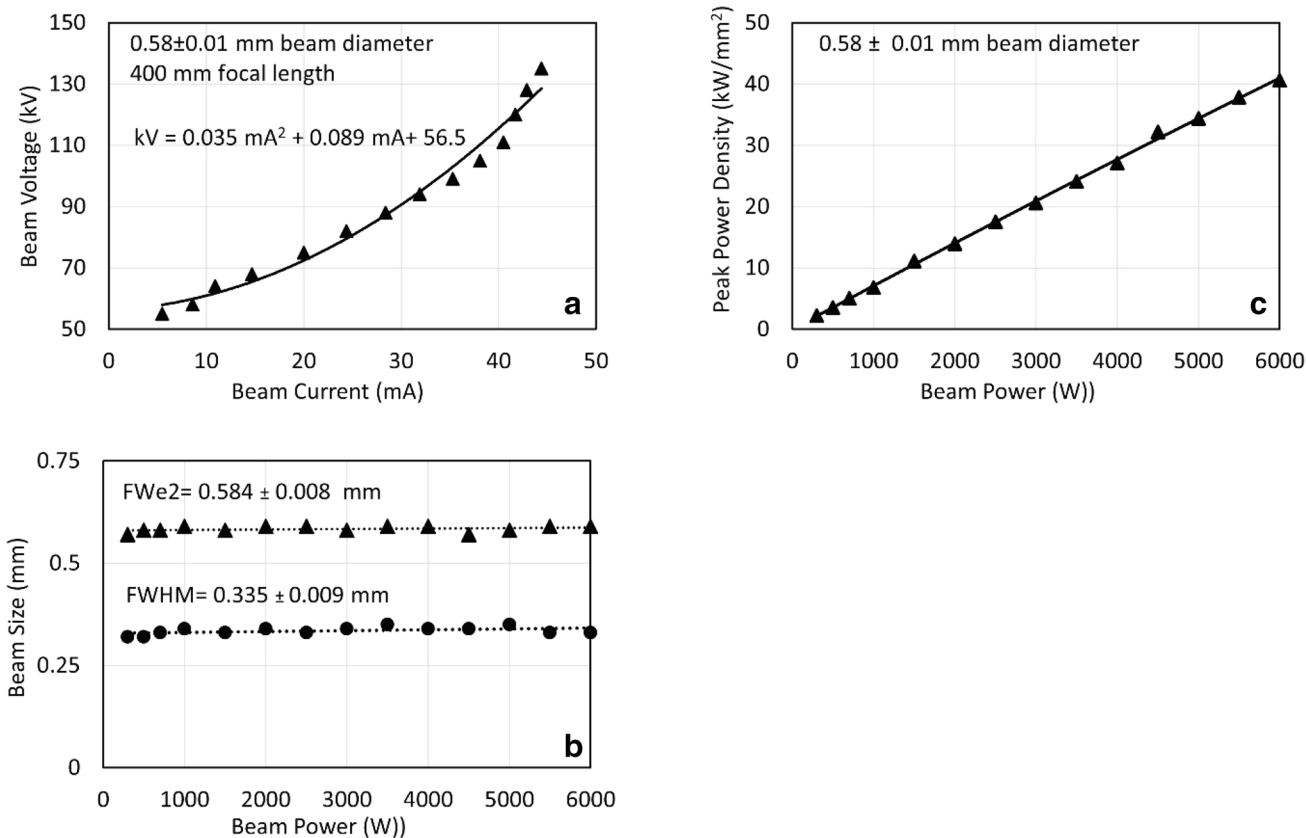
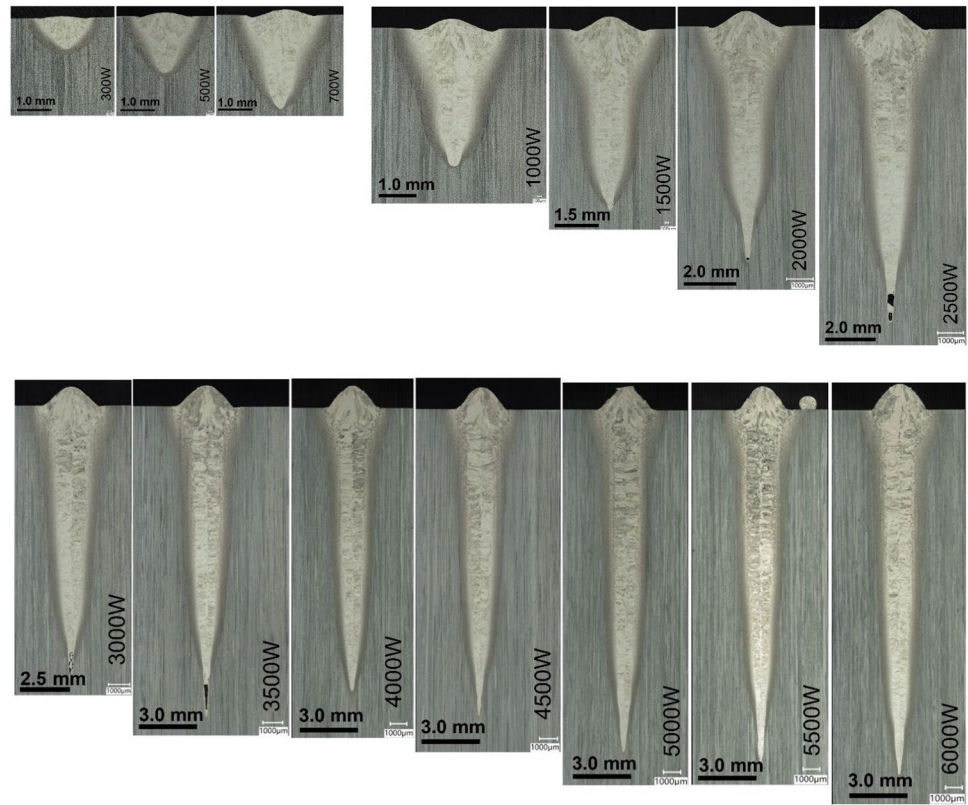


Fig. 11 **a** Relationship between electron beam voltage and beam current required to maintain a constant beam diameter $FWe2=0.58 \text{ mm}$ from 300 to 6000 W power, **b** measured beam size (FWHM and $FWe2$), and **c** measured peak power density as a function of beam power

Fig. 12 Electron beam weld cross sections for the 0.58-mm-diameter beam series of welds at a focal length of 400 mm from 300 to 6000 W. Note the changes in magnification scale markers



penetration keyhole welding conditions. Optical metallography showed no porosity in the weld cross sections, but CT inspection was able to see root porosity in some of the welds. The porosity was always confined to the root of the weld, was more prevalent in the smaller diameter fibers (0.1 and 0.2 mm), and was more prevalent in the higher power welds with high aspect ratios. The 0.3-mm diameter showed no pores at all, throughout the entire range of powers and for both the 400- and 500-mm focal length lenses.

Figure 8a shows CT scans of a 0.39-mm-diameter beam weld with some porosity, which appears as a string of small pores in line at the weld root and is typical of the welds made at 2500 W or higher on the 0.20- and 0.39-mm laser beams. The pore sizes are less than 1 mm and represent significantly less than 1% of the fusion zone volume, and would typically not be considered a problem in a well-designed step joint configuration where the root porosity is buried below the step and into the backing material. This type of porosity is similar to that commonly observed in electron beam keyhole welds, and is related to spiking of the high power density beam at the weld root [2, 65]. CT scans of the reduced pressure laser welds using the 0.3-mm-diameter fiber are shown in Fig. 8b for the 0.58-mm beam (400 mm focusing lens) at 6000 W, and in Fig. 8c for the 0.74-mm (500-mm focusing lens) beam at 6000 W. Neither of these beams developed any porosity over the entire range of powers up to 6000 W, which differentiates them from deep penetration electron beam welds that commonly have root spike defects.

The microstructural features of the laser welds are shown in Figs. 9 and 10. The fusion zone microstructure is comprised mainly of what appears to be acicular α' phase that forms martensitically from the prior β grain boundaries in the fusion zone and grows into the interior of the grains. A slightly coarser Widmanstätten α phase may also be present in places, while residual β exists between the α or α' acicular phase needles or plates. This microstructure is characteristic of rapidly cooled welds such as laser and electron beam, where there is little time for the acicular α or α' phase to coarsen into laths. Figure 9 shows this microstructure at low and high magnifications at both the crown and root of the fusion zone for the 2000-W weld made with the 0.58-mm-diameter beam. In these micrographs, the β phase etches darker than the alpha phase, and the prior β grain boundaries show up where different orientations of the alpha phase meet on either side of the boundary. The prior β grain boundaries are larger and more elongated at the crown compared with the root of the welds, and these microstructural features are similar in all the reduced pressure laser welds examined in this study.

Figure 10a shows the heat-affected zone of this same weld at low magnification, clearly indicating a gradient in microstructure from the fusion zone to the base metal. The microstructure adjacent to the fusion zone boundary was heated above the β transus of approximately 900 °C where complete transformation to β occurred prior to cooling. This microstructure is shown at higher magnifications in Fig. 10b.

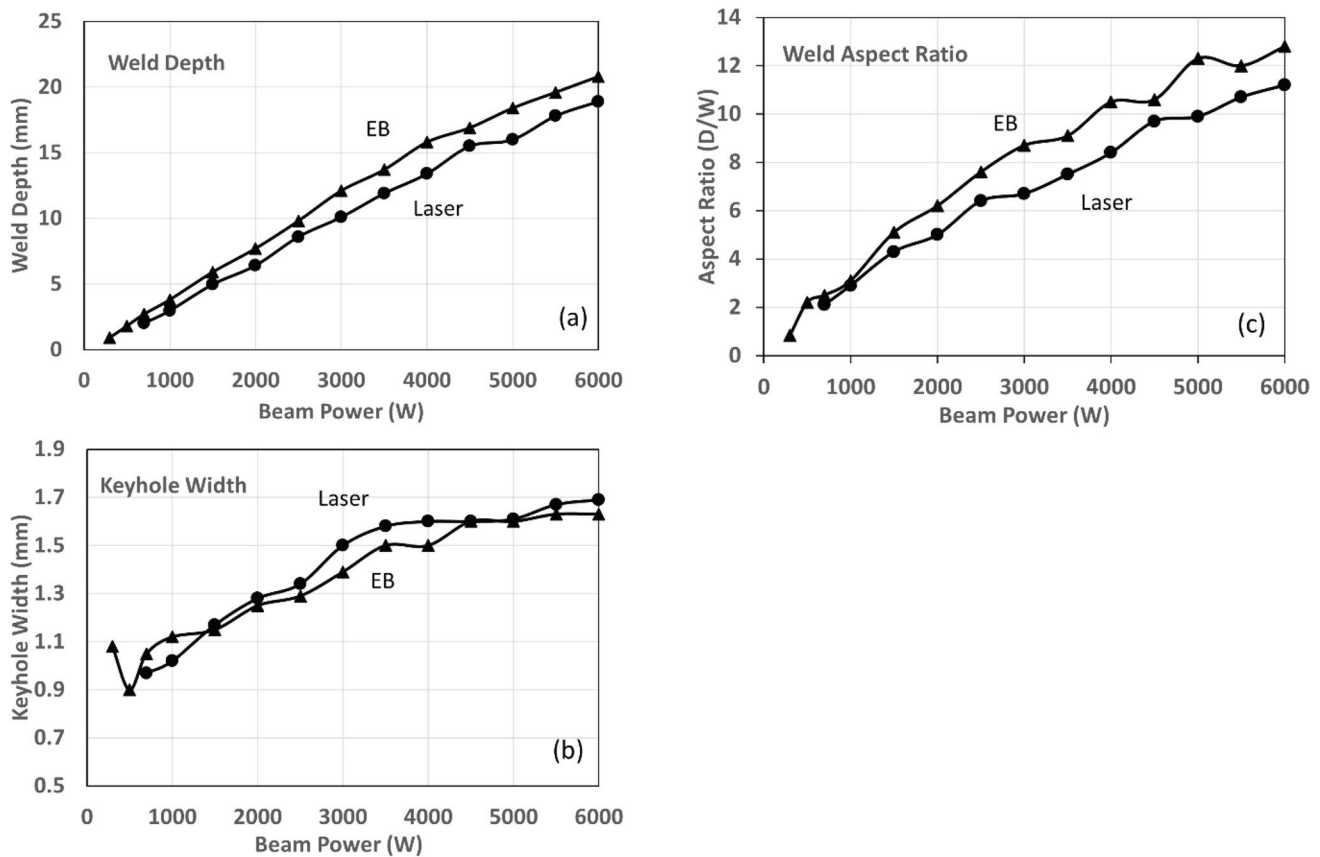


Fig. 13 Comparison of the electron beam and reduced atmosphere laser beam weld cross-sectional shapes for the 0.58-mm-diameter beams plotted versus weld power showing **a** weld penetration, **b** keyhole width, and **c** weld aspect ratio (D/W)

Further away from the fusion boundary, the grains coarsen relative to the base metal and retain some untransformed alpha phase, giving it a similar appearance to the base metal but with a transition in grain size from the coarsened HAZ grains nearer to the fusion boundary to the smaller base metal grains.

3.4 Comparison to electron beam welds

The electron beam power distributions were characterized at a focal length of 500 mm, using different accelerating voltages to create two spot sizes that matched the 0.39-mm and 0.58-mm laser beams. Table 3 summarizes the power density distribution of the two electron beams at a 1-kW power level as measured by the EMFC shows that the 0.39-mm-diameter electron beam has a peak power density (PPD) of $\sim 15,000$ W/mm², and the 0.58-mm-diameter beam has a power density of ~ 7000 W/mm². These peak power densities are approximately $1.5\times$ higher than the top-hat value of the laser beam due to the inherent difference in the power density distributions between fiber laser and the electron beams as shown in Figs. 2 and 3. Additional mapping of the electron beam at 500-mm focal length showed that it

would be difficult to produce a 0.58-mm-diameter beam at the highest power of 6000 W; hence, the electron beam focal length was reduced to 400 mm where it could easily obtain a 0.58-mm beam at all powers from 300 to 6000 W.

Electron beam welds were then made at a focal length of 400 mm to exactly match the 0.58-mm-diameter laser beam throughout the entire power range to match the 0.3-mm laser fiber, 200-mm collimator, and 400-mm focal length lens that had a 0.58-mm beam diameter. To keep the electron beam diameter constant as the beam current increased at a fixed focal length, the accelerating voltage was increased with beam current. Figure 11a plots the relationship between kilovolt and milliamperes for the 14 electron beam welds that were made while keeping the beam diameter FWe2 constant at $0.58\text{ mm} \pm 0.01\text{ mm}$. The results are further summarized in Table 6 and show that beam voltages as low as 55 kV and up to 135 kV were required to maintain the beam diameter from low beam currents of 5.5 mA for the 300-W beam up to the maximum of 44.4 mA for the 6000-W beam.

Figure 11b plots the beam size measurements for the FWHM (beam width at 50% of the peak power density) and FWe2 (beam diameter at $1/e^2$ (13.5%) of the peak power density) for each of the electron beams, while Fig. 11c plots

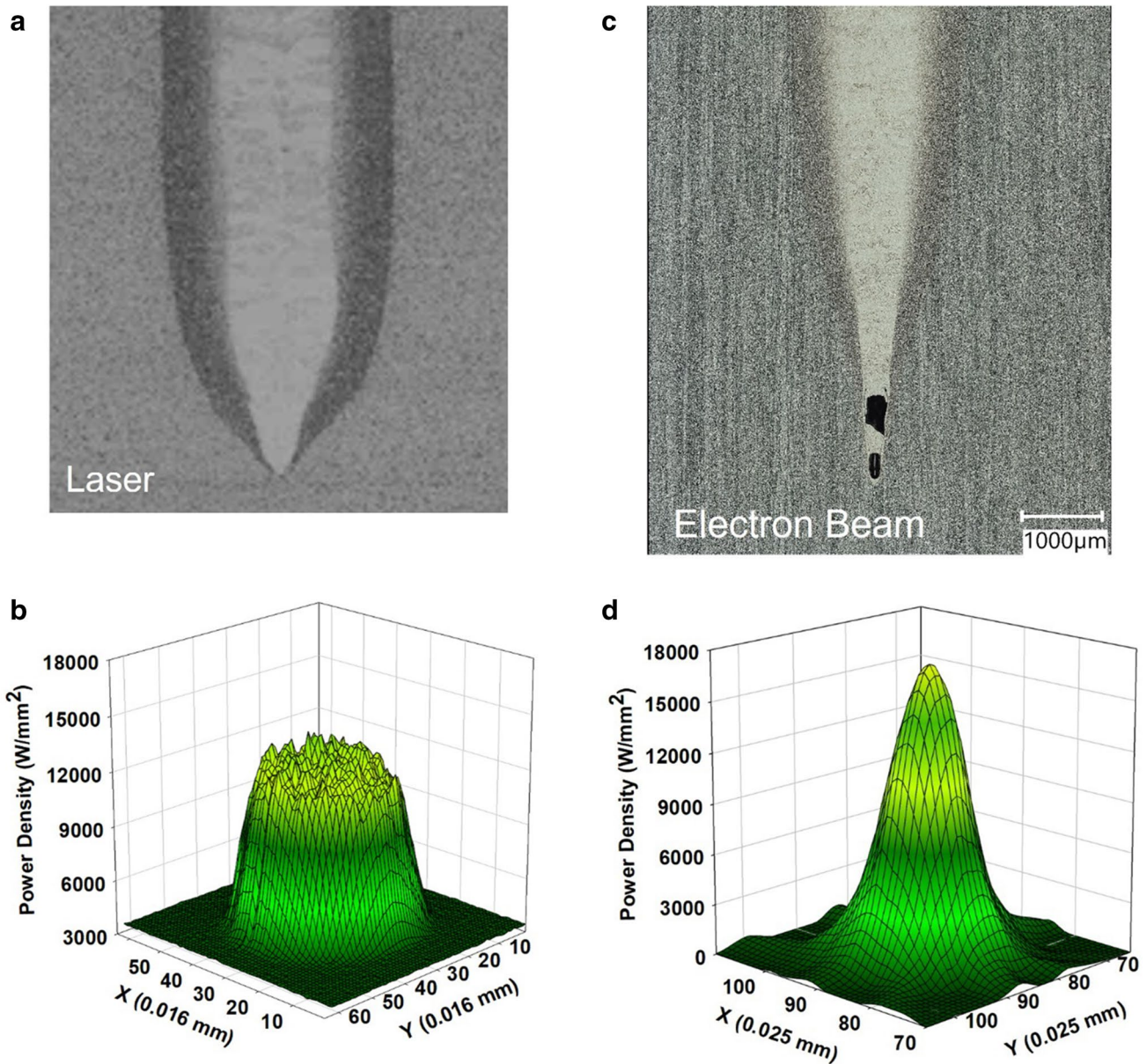


Fig. 14 Weld root cross sections imaged at the same magnification and power density distribution comparison of the electron beam and reduced pressure laser weld at 2500 W for the 0.58-mm-diameter

beams. **a** Laser weld root, **b** laser weld power density distribution, **c** electron beam weld root showing porosity, and **d** electron beam power density distribution

the measured peak power density of each of the beams, showing a linear trend with beam power over the entire range from 2.2 to 40.6 kW/mm² as measured by the EMFC diagnostic. Note that FWHM contains 50% of the beam's power, while FWE2 contains 86.5% of the beam's power and is equivalent to the 4 σ diameter of a circular Gaussian shape used to describe laser beams [66].

Electron beam welds were made at the same speed as the laser welds (15.4 mm/s) with each of the 14 parameters summarized in Table 6 and in Fig. 11. The welds were made in vacuum at 9×10^{-5} mbar, producing clean shiny

metal surfaces with no oxide discoloration. At powers above 2000 W, there was some ejection of small molten droplets from the weld, and above 4000 W there was some humping of the weld bead along its length. The welds were cross sectioned approximately 15 mm from the start of the weld, which is past the initial hump in the plate that is produced prior to the weld keyhole stabilizing. After cross sectioning, polishing, and etching, the welds were photographed and measured for penetration depth and keyhole width. The deeper electron beam welds had a noticeable spike at the root, and the weld depths were measured at approximately

½ of the spike depth due to variability at the root, based on the location of the heat-affected zone which is more prominent above the spike than below it. Figure 12 summarizes the cross sections of these welds that vary in depth from 0.9 to 20.8 mm. The overall geometric shape of the weld fusion zone is different than the laser welds where it is more tapered in the bottom half of the keyhole, creating a more pointed and spikier root. Microstructures of the electron beam welds looked very similar to the reduced pressure laser welds shown in Figs. 9 and 10.

Figure 13 summarizes the EB weld penetration, keyhole width, and weld aspect ratios for each of the electron beam welds and compares these data to the reduced atmosphere laser welds. In these plots, the data are simply plotted versus beam power since the beam diameter (0.58 mm) and weld travel speed (15.4 mm/s) are kept constant for all of the conditions. Figure 13a shows the weld depth versus power, indicating that the electron beam produces a deeper weld by 16% on average ($116 \pm 5.4\%$) than the reduced atmosphere laser welds over the 6-kW power range. The weld widths show similar trends between the EB and laser, with the laser having a bit larger keyhole width in general than the electron beam. The combination of deeper and slightly narrower electron beam weld profiles results in a higher aspect ratio for the electron welds as summarized in Fig. 13c, with aspect ratios greater than 10 for both processes at the highest power levels.

Figure 14 shows a side-by-side comparison of the roots of the reduced atmosphere laser weld and the electron beam weld made at 2500 W with 0.58-mm-diameter beams. It is clear that the electron beam weld is more tapered at the root than the laser weld which maintains its keyhole diameter to penetrations closer to the bottom of the weld. In addition, the electron beam shows a spike and associated root porosity, whereas the laser weld showed no porosity in cross section or in X-ray imaging in any of the 0.58- and 0.74-mm-diameter beam welds. It is believed that the difference in weld profile is related to the Gaussian shape of the electron beam power density distribution which has a more intense peak (Fig. 14d) than the top-hat distribution of the laser beam (Fig. 14b).

In summary, the results presented here demonstrate that deep electron-beam type welds can be made with reduced pressure lasers over a wide range of powers in Ti-6Al-4 V. These welds have deep keyhole geometries with similar aspect ratios as electron beams that operate under high vacuum conditions. The reduced pressure laser system is robust enough to be used for high volume production and has potential advantages over electron beam welding for certain applications due to the relative simplicity of the laser vacuum pumping system with very fast pump down times, and weld quality that matches or exceeds electron beams with minimal root porosity.

4 Conclusions

1. A reduced pressure laser system was specified for production level welding. The laser was used to demonstrate high-quality welds in Ti-6Al-4 V using a mechanically pumped system at 1 mbar (0.1 kPa, 0.75 Torr) pressure that pumps the chamber to welding pressures in less than 1 min. Over 1000 demonstration welds have been made in this system on Ti-6Al-4 V without having to clean or change the laser beam passthrough window or vapor shield.
2. Reduced pressure laser weld depths, widths, and aspect ratios were measured as a function of beam power up to 6 kW. Different optical configurations were used with fibers of 0.1-, 0.2-, and 0.3-mm diameters, and focusing lenses of 400 and 500 mm, which produced measured spot size diameters of 0.20, 0.39, 0.58, and 0.74 mm. Deep keyhole welding was observed in all of the welds, with narrow keyhole walls, D/W aspect ratios as high as 17:1, and penetration depths to 20 mm.
3. The penetration data for all of the reduced pressure laser welds were fit to a power factor relationship (see Eq. 1) to account for different beam diameters. The fit had a high statistical R^2 confidence of 0.989 for the prediction of weld depth over a wide range of conditions and penetrations from 1 to 20 mm. This relationship can be used to aid in design of future systems to optimize power and optical configurations for reduced pressure laser beam welding conditions.
4. Electron beam welds were developed to match the 0.58-mm-diameter laser beam, which required an increasing electron beam voltage to maintain a constant beam size as the beam current was increased. The electron beam welds were made at 9×10^{-5} mbar (6.8×10^{-5} Torr) and follow similar penetration trends to the reduced pressure laser welds made at 1 mbar, with electron beam welds being $16 \pm 5.4\%$ deeper than the laser welds throughout the entire power range. The deeper penetration of the electron beam welds is likely related to the more spiked Gaussian-like power distribution of the electron beam which has about $1.5 \times$ higher peak power density than the top-hat distribution of the multi-mode laser at a given power and beam diameter.
5. The quality of reduced pressure laser welds was observed by cross sectioning and X-ray analysis and showed that only a few isolated pores were present in the reduced atmosphere laser welds made with the 0.20- and 0.39-mm-diameter beams, while no porosity was observed in any of the 0.58- and 0.74-mm-diameter beams for all powers up to 6000 W. However, cross sections of the electron beam welds made with a 0.58-mm beam diameter showed typical root porosity at powers of 1.5 kW and higher.

Appendix

Table 5 Summary of reduced pressure laser weld penetrations, widths, and aspect ratios for Ti-6Al-4 V at 15.4 mm/s

Power (W)	0.20-mm beam			0.39-mm beam			0.58-mm beam			0.74-mm beam		
	Depth (mm)	Width (mm)	D/W -	Depth (mm)	Width (mm)	D/W -	Depth (mm)	Width (mm)	D/W -	Depth (mm)	Width (mm)	D/W -
200	0.9	0.57	1.58									
300	1.58	0.63	2.51									
400	2.38	0.68	3.5									
500	3.17	0.71	4.46									
600	3.96	0.72	5.5									
700	4.88	0.74	6.59	2.42	0.84	2.9	2.03	0.97	2.1	1.99	1.21	1.6
800	5.54	0.79	7.01									
900	6.1	0.82	7.44									
1000	6.9	0.89	7.75	3.8	0.88	4.30	2.98	1.02	2.9	2.8	1.21	2.3
1500				6.0	0.92	6.52	4.98	1.17	4.3	4.4	1.29	3.4
2000				7.5	1.03	7.28	6.42	1.28	5.0	6.2	1.38	4.5
2500				9.0	1.07	7.28	8.6	1.34	6.4	7.5	1.38	5.4
3000				12.0	1.15	10.4	10.1	1.5	6.7	9.1	1.48	6.1
3500				13.3	1.15	11.6	11.9	1.58	7.5	11.3	1.87	6
4000				15.4	1.15	13.4	13.4	1.6	8.4	13.1	1.89	6.9
4500				16.3	1.16	14.1	15.5	1.6	9.7	14.1	1.86	7.6
5000				18.3	1.17	15.6	16.0	1.61	9.9	15.3	1.78	8.6
5500				19.1	1.16	16.5	17.8	1.67	10.7	16.1	1.78	9
6000				19.4	1.14	17.0	18.9	1.69	11.2	17.6	1.75	10.1

Table 6 Summary of electron beam weld and beam parameters, weld penetrations, keyhole widths, and weld aspect ratios for Ti-6Al-4 V. All welds made at 15.4 mm/s using a 0.58-mm-diameter beam with an effective focal length of 400 mm

Beam power (W)	Beam voltage (kV)	Beam current (mA)	Beam peak power density (W/mm ²)	Beam width FWHM (mm)	Beam diam- eter FWe2 (mm)	Weld depth (mm)	Keyhole width at half-depth (mm)	Weld aspect ratio D/W -
300	55	5.5	2200	0.32	0.57	0.9	1.08	0.83
500	58	8.6	3500	0.32	0.58	1.8	0.9	2.2
700	64	10.9	5020	0.33	0.58	2.7	1.05	2.5
1000	68	14.7	6800	0.34	0.59	3.8	1.12	3.1
1500	75	20.0	11,100	0.33	0.58	5.9	1.15	5.1
2000	82	24.4	13,900	0.34	0.59	7.7	1.25	6.2
2500	88	28.4	17,500	0.33	0.59	9.8	1.29	7.6
3000	94	31.9	20,600	0.34	0.58	12.1	1.39	8.7
3500	99	35.3	24,100	0.35	0.59	13.7	1.5	9.1
4000	105	38.1	27,100	0.34	0.59	15.8	1.5	10.5
4500	111	40.5	32,200	0.34	0.57	16.9	1.6	10.6
5000	120	41.7	34,400	0.35	0.58	18.4	1.6	12.3
5500	128	42.9	37,800	0.33	0.59	19.6	1.63	12.0
6000	135	44.4	40,600	0.33	0.59	20.8	1.63	12.8

Acknowledgements The LLNL portion of this work was performed under the auspices of the US Department of Energy by Lawrence Livermore National Laboratory under Contract DE-AC52-07NA27344. The authors would like to thank the following contributors for their work. John Sengthay of LLNL for preparation of the electron beam weld metallographic cross sections; Ian Duckett, Terry Stothard, and Dan Cuthbertson from InnoLas UK Ltd for manufacturing the ILIV 420 System and supporting the laser welding trials; and, from AWE, Jessica Opie for performing CT radiography and reconstruction of the data, Neil Bond for preparing the metallographic samples, and Andrew Johnson for preparation of the laser welding figure.

Declarations

Competing interests The authors declare no competing interests.

Open Access This article is licensed under a Creative Commons Attribution 4.0 International License, which permits use, sharing, adaptation, distribution and reproduction in any medium or format, as long as you give appropriate credit to the original author(s) and the source, provide a link to the Creative Commons licence, and indicate if changes were made. The images or other third party material in this article are included in the article's Creative Commons licence, unless indicated otherwise in a credit line to the material. If material is not included in the article's Creative Commons licence and your intended use is not permitted by statutory regulation or exceeds the permitted use, you will need to obtain permission directly from the copyright holder. To view a copy of this licence, visit <http://creativecommons.org/licenses/by/4.0/>.

References

- Elmer JW, Hohanadel PW, Lachenberg K, Caristan C, Webber T. in *ASM handbook of welding* Vol. 11 522–539 (ASM International, 2011)
- Patterson T, Hohanadel J, Sutton S, Pantan B, Lippold J (2021) A review of high energy density beam processes for welding and additive manufacturing applications. *Welding in the world* 65:1235–1306. <https://doi.org/10.1007/s40194-021-01116-0>
- Schultz H (1994) *Electron beam welding*, 1st edn. Woodhead Publishing, Sawston
- The Welding Institute, Web-page on in-chamber electron beam welding* (The Welding Institute, Granta Park, Cambridge CB21 6AL, 2022)
- v. Drobneck D (2005) *Electron Beam Welding*. Pro-Beam, Germany. Examples of 30 Years Job-Shop Experience, available from Pro-Beam, www.pro-beam.com
- Swifhook DT, Gick AEF (1973) Penetration welding with lasers. *Weld J* 52:S492–S492
- Arata Y, Abe N, Oda T (1985) Fundamental phenomena in high power CO₂, report II, vacuum laser welding. *Trans JWRI* 14:217–222
- Verwaerde A, Fabbro R, Deshors G (1995) Experimental-study of continuous CO₂-laser welding at subatmospheric pressures. *J Appl Phys* 78:2981–2984. <https://doi.org/10.1063/1.360046>
- Kabasawa M, Ono M, Nakada K, Kosuge S (1992) Effect of ambient pressure and shielding gas on penetration depth and CO₂ laser-induced plasma behavior. *Proceedings of the european conference on laser treatment of materials ECLAT*, Gottingen, Germany, pp 667–672
- Katayama S, Kobayashi Y, Mizutani M, Matsunawa A (2001) Effect of vacuum on penetration and defects in laser welding. *J Laser Appl* 13:187–192. <https://doi.org/10.2351/1.1404413>
- Katayama S, Yohei A, Mizutani M, Kawahito Y. in *Lasers in manufacturing 2011: Proceedings of the Sixth International WIT Conference on Lasers in Manufacturing, Vol 12, Pt A* Vol. 12 *Physics Procedia* (eds M. Schmidt, M. Zaeh, T. Graf, & A. Ostendorf) 75–80 (Elsevier Science Bv, 2011)
- Web-of-Science Clairvate Analytics (2021) Title search for “Laser Welding”, “Electron Beam Welding” and “Laser Welding under Reduced Pressure or Vacuum” patents were not included in the search
- Jiang M, Tao W, Chen Y (2017) Laser welding under vacuum: a review. *Appl Sci* 7:909
- Fabbro R, Hirano K, Pang SY (2016) Analysis of the physical processes occurring during deep penetration laser welding under reduced pressure. *J Laser Appl* 28:7. <https://doi.org/10.2351/1.4944002>
- Peng GC, Li LQ, Xia HB, Gong JF (2018) in *Numisheet 2018: 11th International Conference and Workshop on Numerical Simulation of 3d Sheet Metal Forming Processes* Vol. 1063 *J Phys Conf Ser* (eds T. Kuwabara *et al.*)
- Youhei A *et al* (2014) Effect of reduced pressure atmosphere on weld geometry in partial penetration laser welding of stainless steel and aluminium alloy with high power and high brightness laser. *Sci Technol Weld Join* 19:324–332. <https://doi.org/10.1179/1362171813y.0000000182>
- Teichmann F, Mueller S, Dilger K (2018) Investigations on dual laser beam welding of aluminum high pressure die castings at reduced ambient pressure. *J Laser Appl* 30. <https://doi.org/10.2351/1.5040640>
- Pang SY, Hirano K, Fabbro R, Jiang T (2015) Explanation of penetration depth variation during laser welding under variable ambient pressure. *J Laser Appl* 27:8. <https://doi.org/10.2351/1.4913455>
- Rominger V, Berger P, Huegel H (2019) Effects of reduced ambient pressure on spattering during the laser beam welding of mild steel. *J Laser Appl* 31. <https://doi.org/10.2351/1.5007186>
- Francis JA *et al.* (2019) Vacuum laser welding of SA508 steel. *Journal of Materials Processing Technology* 274. <https://doi.org/10.1016/j.jmatprotec.2019.116269>
- Yang S, Wang J, Carlson BE, Zhang J (2013) Vacuum-assisted laser welding of zinc-coated steels in a gap-free lap joint configuration. *Weld J* 92:197S-204S
- Wang C, Lei B, Jiang P, Xu X, Mi G (2018) Numerical and experimental investigation of vacuum-assisted laser welding for DP590 galvanized steel lap joint without prescribed gap. *Int J Adv Manuf Technol* 94:4177–4185. <https://doi.org/10.1007/s00170-017-1067-6>
- Reisgen U, Olschok S, Turner C (2017) Welding of thick plate copper with laser beam welding under vacuum. *J Laser Appl* 29. <https://doi.org/10.2351/1.4983165>
- Elmer JW, Vaja J, Carlton HD (2016) The effect of reduced pressure on laser keyhole weld porosity and weld geometry in commercially pure titanium and nickel. *Weld J* 95:419S-430S
- Li L, Peng G, Wang J, Gong J, Li H (2018) Experimental study on weld formation of Inconel 718 with fiber laser welding under reduced ambient pressure. *Vacuum* 151:140–147. <https://doi.org/10.1016/j.vacuum.2018.02.008>
- Jun H-J, Yun CG, Joo JH, Lee HJ, Lee KS (2019) Properties of vacuum-laser-welded Ti-based bulk metallic glass and Zr-based bulk metallic glass composite. *Int J Mater Res* 110:648–655. <https://doi.org/10.3139/146.111782>
- Jakobs S, Reisgen U (2015) Laser beam welding under reduced pressure - range of possible applications for thick-plates. *Stahlbau* 84:635–642. <https://doi.org/10.1002/stab.201510306>
- Sokolov M, Salminen A, Katayama S, Kawahito Y (2015) Reduced pressure laser welding of thick section structural steel. *J Mater Process Technol* 219:278–285. <https://doi.org/10.1016/j.jmatprotec.2014.12.026>

29. Katayama S, Kawahito Y, Mizutani M. in *Laser assisted net shape engineering 7* Vol. 39 *Physics Procedia* (eds M. Schmidt, F. Vollertsen, & M. Geiger) 8–16 (Elsevier Science Bv, 2012)
30. Jiang M, Chen YB, Debroy T (2020) Enhanced penetration depth during reduced pressure keyhole-mode laser welding modeling and experiments took place to understand deeper laser keyholes at lower pressures. *WELD J* 99:110–123. <https://doi.org/10.29391/2020.99.011>
31. Jiang M, Chen X, Chen Y, Tao W (2020) Mitigation of porosity defects in fiber laser welding under low vacuum. *J Mater Process Technol* **276**, <https://doi.org/10.1016/j.jmatprotec.2019.116385>
32. Teichmann F, Mueller S, Dilger K (2018) in *10th Cirp Conference on Photonic Technologies [Lane 2018]* Vol. 74 *Procedia CIRP* (eds M. Schmidt, F. Vollertsen, & G. Dearden) 438–441
33. Seto N, Katayama S, Matsunawa A (2000) High-speed simultaneous observation of plasma and keyhole behavior during high power CO2 laser welding: effect of shielding gas on porosity formation. *J Laser Appl* 12:245–250. <https://doi.org/10.2351/1.1324717>
34. Lin RQ, Wang HP, Lu FG, Solomon J, Carlson BE (2017) Numerical study of keyhole dynamics and keyhole-induced porosity formation in remote laser welding of Al alloys. *Int J Heat Mass Transf* 108:244–256. <https://doi.org/10.1016/j.ijheatmasstransfer.2016.12.019>
35. Norris JT, Robino CV, Hirschfeld DA, Perricone MJ (2011) Effects of laser parameters on porosity formation: investigating millimeter scale continuous wave Nd:YAG laser welds. *Weld J* 90:198S–203S
36. Kuo T-Y, Lin Y-D (2007) Effects of different shielding gases and power waveforms on penetration characteristics and porosity formation in laser welding of Inconel 690 alloy. *Mater Trans* 48:219–226. <https://doi.org/10.2320/matertrans.48.219>
37. Fabbro R (2019) Scaling laws for the laser welding process in keyhole mode. *J Mater Process Technol* 264:346–351. <https://doi.org/10.1016/j.jmatprotec.2018.09.027>
38. Fabbro R (2020) Depth dependence and keyhole stability at threshold, for different laser welding regimes. *Appl Sci-Basel* **10**, <https://doi.org/10.3390/app10041487>
39. Greses J, Hilton PA, Barlow PA, Steen WM (2004) Plume attenuation under high power Nd : yttrium-aluminum-garnet laser welding. *J Laser Appl* 16:9–15. <https://doi.org/10.2351/1.1642636>
40. Lacroix D, Jeandel G, Boudot C (1998) Solution of the radiative transfer equation in an absorbing and scattering Nd:YAG laser-induced plume. *J Appl Phys* 84:2443–2449. <https://doi.org/10.1063/1.368405>
41. Matsunawa A, Semak V (1997) The simulation of front keyhole wall dynamics during laser welding. *J Phys D-Appl Phys* 30:798–809. <https://doi.org/10.1088/0022-3727/30/5/013>
42. Rai R, Burgardt P, Milewski JO, Lienert TJ, DebRoy T (2008) Heat transfer and fluid flow during electron beam welding of 21Cr–6Ni–9Mn steel and Ti–6Al–4V alloy. *J Phys D Appl Phys* 42:025503. <https://doi.org/10.1088/0022-3727/42/2/025503>
43. Jiang M, Chen YB, Chen X, Toa W, Debroy T (2020) Enhanced penetration depth during reduced pressure keyhole-mode laser welding modeling and experiments took place to understand deeper laser keyholes at lower pressures. *Weld J* 99:110–123. <https://doi.org/10.29391/2020.99.011>
44. Jiang M, Chen X, Chen Y, Tao W (2019) Increasing keyhole stability of fiber laser welding under reduced ambient pressure. *J Mater Process Technol* 268:213–222. <https://doi.org/10.1016/j.jmatprotec.2019.01.026>
45. Han S-W, Cho W-I, Zhang L-J, Na S-J (2021) A study on laser keyhole welding in vacuum by computational fluid dynamics simulations with plume effect models. *J Laser Appl* **33**, <https://doi.org/10.2351/7.0000235>
46. PTR PT (2021) *Laser welding in vacuum: LASVAC welding system | PTR-Precision Technologies, Inc. (ptreb.com)*; <<https://www.ptreb.com/welding-systems/vacuum-laser-welding-systems>>. Accessed January 2022
47. ProBeam G (2021) *Laser welding - Gearline Laser: pro-beam*; <<https://www.pro-beam.com/en/systems/weldingsystems-for-high-throughput/gearlinelaser/>>. Accessed January 2022
48. Focus (2021) *Laser welding under vacuum: LaVa - FOCUS E-Welding (focus-e-welding.de)*; <<https://www.focus-e-welding.de/laser-welding-under-vacuum/>>. Accessed January 2022
49. Cambridge, Vacuum & Engineering (2021) *Laser In Vacuum*; <<https://camvaceng.com/machine/laser-welding-in-vacuum-machines/>>. Accessed January 2022
50. Lee Y, Cheon J, Min B-K, Kim C (2019) Contamination of coupling glass and performance evaluation of protective system in vacuum laser beam welding. *Appl Sci-Basel* **9**, <https://doi.org/10.3390/app9235082>
51. Elmer JW, Vaja J, Carlton HD, Pong R (2015) The effect of Ar and N-2 shielding gas on laser weld porosity in steel, stainless steels, and nickel. *Weld J* 94:313S–325S
52. The laser coupling system was licensed by InnoLas from ISF Aachen, G. (2021)
53. Palmer TA, Elmer JW (2007) Characterization of electron beams at different focus settings and work distances in multiple welders using the enhanced modified Faraday cup. *Sci Technol Weld Join* 12(2):161–174. <https://doi.org/10.1179/174329307X176631>
54. Elmer JW, Teruya AT (2001) An enhanced Faraday cup for the rapid determination of the power density distribution in electron beams. *Weld J* 80(12):288s–295s
55. Elmer W, Teruya AT, O'Brien DW (1993) Tomographic imaging of non-circular and irregular electron beam power density distributions. *Weld J* 72(11):493s–505s
56. Elmer JW, Teruya AT (1998) Fast method for measuring power density distribution of non-circular and irregular electron beams. *Sci Technol Weld Join* 3:51–58. <https://doi.org/10.1179/stw.1998.3.2.51>
57. Eagar T, Tsai N (1983) Temperature fields produced by traveling distributed heat sources. *Weld J* 62:346–355
58. Fabbro R (2010) Melt pool and keyhole behaviour analysis for deep penetration laser welding. *J Phys D Appl Phys* 43:445501. <https://doi.org/10.1088/0022-3727/43/44/445501>
59. Elmer JW, Giedt WH, Eagar TW (1990) The transition from shallow to deep penetration during electron-beam welding. *Weld J* 69:167–s
60. Miyazaki T, Giedt WH (1982) Heat-transfer from an elliptical cylinder moving through an infinite-plate applied to electron-beam welding. *Int J Heat Mass Transf* 25:807–814
61. Rai R, Elmer JW, Palmer TA, DebRoy T (2007) Heat transfer and fluid flow during keyhole mode laser welding of tantalum, Ti–6Al–4V, 304L stainless steel and vanadium. *J Phys D-Appl Phys* 40:5753–5766. <https://doi.org/10.1088/0022-3727/40/18/037>
62. Rai R, Palmer T, Elmer JW, DebRoy T (2009) Heat transfer and fluid flow during electron beam welding of 304L stainless steel alloy. *Weld J* 88:54s–61s
63. He X, Elmer JW, DebRoy T (2005) Heat transfer and fluid flow in laser microwelding. *J APPL PHYS* **97**, <https://doi.org/10.1063/1.1873032>
64. DebRoy T et al (2018) Additive manufacturing of metallic components – process, structure and properties. *Prog Mater Sci* 92:112–224. <https://doi.org/10.1016/j.pmatsci.2017.10.001>
65. Wei PS, Chuang KC, Ku JS, DebRoy T (2012) Mechanisms of spiking and humping in keyhole welding. *IEEE Trans Compon Pack Manuf Technol* 2:383–394. <https://doi.org/10.1109/tcpmt.2011.2178412>
66. ISO Standard 11146–1:2021(E) Part 1: stigmatic and simple astigmatic beams (2021) *Lasers and laser-related equipment — Test methods for laser beam widths, divergence angles and beam propagation ratios*. Organization for Standardization, Geneva

Publisher's Note Springer Nature remains neutral with regard to jurisdictional claims in published maps and institutional affiliations.